

CrystEngComm

Accepted Manuscript



This is an *Accepted Manuscript*, which has been through the Royal Society of Chemistry peer review process and has been accepted for publication.

Accepted Manuscripts are published online shortly after acceptance, before technical editing, formatting and proof reading. Using this free service, authors can make their results available to the community, in citable form, before we publish the edited article. We will replace this *Accepted Manuscript* with the edited and formatted *Advance Article* as soon as it is available.

You can find more information about *Accepted Manuscripts* in the [Information for Authors](#).

Please note that technical editing may introduce minor changes to the text and/or graphics, which may alter content. The journal's standard [Terms & Conditions](#) and the [Ethical guidelines](#) still apply. In no event shall the Royal Society of Chemistry be held responsible for any errors or omissions in this *Accepted Manuscript* or any consequences arising from the use of any information it contains.



ARTICLE

Energy efficient, microwave-hydro-/solvothermal synthesis of hierarchical flowers and rice-grain like ZnO nanocrystals as photoanodes for high performance dye-sensitized solar cells

Received 00th January 20xx,
Accepted 00th January 20xx

DOI: 10.1039/x0xx00000x

www.rsc.org/

R. Krishnapriya, S. Praneetha and A. Vadivel Murugan*

ZnO with different morphologies including marigold flower like (MGFL), multipod-jasmine flower like (MPJF), sea urchin-rod flower like (URFL), calendula flower like (CDFL) and rice-grain-shape like (RGSL) nanoparticles were successfully synthesized by decomposing either $\text{Zn}(\text{OH})_4^{2-}$ or $\text{Zn}(\text{NH}_3)_4^{2+}$ precursor precursor in different solvents such as H_2O , ethylene glycol (EG) and ethanol (EtOH) *via* one-pot rapid microwave assisted hydro-/solvothermal (MW-HT/ST) methods. From the obtained ZnO, we have developed two types of innovative photoanode configurations such as “nano-hybrid architecture” and “bi-layer architecture” *via* integration and layer-by-layer coating of flower-like URFL-ZnO and RGSL-ZnO nanoparticles respectively for dye sensitized solar cells (DSSC). Interestingly, the URFL/RGSL-ZnO nano-hybrid architecture photoanode-based DSSCs showed remarkably enhanced power conversion efficiency (PCE) as high as 5.64% compare to their individual components such as flowers-like URFL-ZnO and RGSL-ZnO nanoparticles based DSSCs exhibit PCEs of 2.05% and 0.95% respectively. In contrast, two types of “bi-layer architecture” photoanodes were made up of RGSL-ZnO layer on top of the URFL-ZnO and vice versa were exhibited PCEs of 1.74% and 2.26% respectively. It is revealed that the “hybrid architecture” exhibits superior enhancement in PCE when compared to the “bi-layer architecture” assembly and their respective individual bare ZnO components which was mainly attributed to the synergistic effect of two different morphologies when blended together at a “nanoscale” level. Indeed, superior light-scattering ability and anchoring of more dye molecules was provided by the URFL-ZnO. The fast electron transport through better inter-particle and electronic contacts with fluorine-doped SnO_2 glass (FTO) substrate was facilitated by RGSL-ZnO nanoparticles. Hence, the present investigation facilitates a promising way to enhance the efficiency in ZnO-based DSSC by tuning different morphologies with innovative device architecture.

Introduction

Due to the rapid exhaustion of fossil fuels and increasing global energy demands, development of alternative, sustainable and clean energy technologies has become a necessity to address these inevitable challenges. In this regard, finding a method to convert enormous sunlight into electrical energy has happened to be appealing to satisfy world energy demand. DSSC is a modern electrochemical energy conversion device that was inspired from nature by the breakthrough work of O'Regan and Gratzel in 1991.¹ Considerable attention has been made to

the development of DSSC, owing to their simple fabrication procedures coupled with relatively high power conversion efficiency, eco-friendliness and low cost production.²⁻⁴ So far, DSSC fabricated with TiO_2 nanoparticles have accomplished overall conversion efficiency above 13%.⁵ In the meantime, other n-type semiconducting oxides, such as ZnO, SnO_2 and etc., have been identified as promising photoanodes for DSSC.⁶ Among them different nanostructured morphologies of ZnO have been investigated intensively due to its comparable 3.37 eV band gap and facile synthesis methods. Moreover, there are some significant advantages of ZnO over TiO_2 because it possesses higher electronic mobility that would facilitates fast electron transport followed by reduced recombination loss.^{7,8} Typically excellent light scattering, fast electron transport and high specific surface area properties play an important role in enhancing the light conversion efficiency of the DSSC. Worldwide, researchers have focused on the improvement in light utilization efficiency.⁹⁻¹¹ Another approach has been used for narrowing the band gap of semiconducting metal oxides by imposing defects or impurities to promote visible light absorption.¹²⁻¹⁵ In addition, the Mie scattering effect (periodical perturbation in the electron cloud) of spherical micron size particles has also been demonstrated to elongate

†Advanced Functional Nanostructured Materials Laboratory, Centre for Nanoscience and Technology, Madanjeet School of Green Energy Technologies, Pondicherry University (A Central University), Dr. R. V. Nagar, Kalapet, Puducherry-605014, India. E-mail: avmrjeshwar@gmail.com; avmurugan.nst@pondiuni.edu.in.

Electronic Supplementary Information (ESI) available: Table showing experimental data of different ZnO morphologies and their grain sizes calculated by using Scherrer's equation and figures shows XRD pattern of hybrid photoanode films coated on FTO, Raman spectra of individual and hybrid ZnO, magnified FE-SEM images of ZnO flowers and BET-surface area measurements. Tauc plot from diffuse reflectance spectra of the different hierarchical ZnO flowers, combined J-V curve of the different hierarchical individual ZnO flowers as well as hybrid photoanode films. See DOI: 10.1039/x0xx00000x

the path of the incident light for enhancing the light harvesting efficiency.^{16,17} It is reported that TiO₂ photoanode made up of ≤ 20 nm sized particles with large surface area is beneficial for better dye loading.^{1,3} However, such nanosize particles are lesser than the wavelength of visible light and the transparent film shows inferior photoelectric conversion efficiency.¹⁰ Although improvement in efficiency was demonstrated by using ≥ 50 nm large particles due to better light scattering properties, further enhancement in efficiency was restricted owing to smaller surface area provided by large particles that leads to inferior dye adsorption ability. To address these issues, a novel class of photoanode materials that could be made by tuning of micro to nanometer sizes and different morphologies are expected to provide their specific advantages.¹⁸⁻²² Zheng *et al* constructed bi-layered ZnO nanorod and nanocrystallites photoanode for DSSC and a high conversion efficiency of 4% was achieved.²³ Puyoo *et al* reported photoconversion efficiency of 4.7% for ZnO composite electrode which was much higher than that of bare nanowire or nanoparticles-based DSSC due to the synergistic effects of the nanostructured particles with higher surface area for more dye loading and the nanowire providing electron lifetime extension and light harvesting.²⁴ Recently, Zhu *et al* fabricated different morphologies of ZnO nanocrystals including hollow microspheres, microrods and hierarchical microspheres based DSSC that displayed efficiency of 0.41, 0.79, and 1.42% respectively.²⁵ Over the past decades, considerable efforts have been devoted with great research interest to prepare different hierarchical ZnO nanostructured photoanodes by various physical and chemical methods that had been employed because of the device performance that are dependent on their structure and morphology.²⁶⁻²⁹ Jiang *et al* and Cheng *et al* have reported hierarchical nano-flower by hydrothermal method which showed 1.5% efficiency.^{30,31} Although various hierarchical ZnO microstructures were synthesized and reported by using a variety of organic additives, but less power conversion efficiencies were observed because organic additive molecules were absorbed on the surface of ZnO and thus the efficient surface area decreases.³² Recently, Ko *et al* reported a photoanode fabricated within 3 – 7 hours using organic template-assisted hydrothermally grown ZnO nanoforest and showed a maximum efficiency of 2.63%.³³ Therefore it is necessary to develop suitable synthetic methods to prepare the hierarchical micro-/nanostructured ZnO assembled by nanosheets/rods/particles with a large number of unconventional planes that are desirable as it attributes for significant increase in PCE of DSSC. Particularly, microwave-assisted synthesis has gained greater importance in recent years and represents an eco-friendly process that may be considered as a comparatively low cost, energy efficient, short reaction time (many hours to few minutes) and clean method.³⁴ MW-HT/ST synthesis methods have been reported to accelerate the reaction rates and improve the product yield.^{35,36}

On the basis of the consideration, we reported controllable rapid synthesis of ZnO micro-/nanostructures with different flower-like morphologies including marigold-flowerlike (MGFL), multipod-jasmine-flowerlike (MPJF), urchin-rod-flowerlike (URFL), calendula-flowerlike (CDFL) and rice-grain-shape like (RGSL) morphologies by facile, relatively low-temperature (50 – 180°C) and low cost, energy efficient MW-HT/ST processes within few minutes. The photovoltaic (PV) properties of various morphologies of ZnO-based DSSC were investigated. The PV performances of the three-dimensional bare hierarchical ZnO flower photoanodes were presented with a strong morphology-induced PV performance compared with bare RGSL-ZnO nanoparticles based structures. To the best of our knowledge, this is the first time that the integration of different flower like morphologies of ZnO with rice-grain like ZnO nanoparticles blended in with different mass ratio at nanoscale level as “hybrid architecture” prepared *via* MW-HT/ST methods and its application to DSSCs has been reported. For comparative purpose we also investigated PV performance of flower-like ZnO on top of rice grain like ZnO morphology and *vice-versa* fabricated as “bi-layer architecture”. It is revealed that the PV performances of ZnO photoanodes in “hybrid architecture” were greatly improved when compared to “bi-layer architecture” and individual bare flower like as well as rice grain like ZnO. The enhancement in PV performance of ZnO in “hybrid architecture” owing to increase in light-scattering, the anchoring of more dye molecules due to large specific area and efficient electron transport properties of hybrid flowers like ZnO and rice grain like ZnO nanoparticles aggregates mixing in appropriate mass ratio. In addition the electron-hole recombination would be effectively suppressed as a consequence of fast interfacial charge transfer between different structures in hybrid architecture.

EXPERIMENTAL SECTION

Synthesis and Structural Characterization of ZnO

The microwave-assisted solution growth synthesis (MW-HT/ST) of ZnO was carried out by using Zn(CH₃COO)₂·2H₂O, Zn(NO₃)₂·6H₂O, Zinc metal powder, ethylene glycol, absolute ethanol, NaOH, and ammonium hydroxide that were purchased from SdFine chemicals, Fisher Scientific, Nice, and Himedia chemicals, used as received without further purification. All the experiments were conducted with double distilled water, ethanol, and ethylene glycol. [Zn(NH₃)₄]²⁺ precursor solution was prepared by mixing of 0.5 mol/L zinc acetate dihydrate (Zn(CH₃COO)₂·2H₂O) and fresh ammonia solutions (volume ratio, v/v 1:1, pH~10), whereas [Zn(OH)₄]²⁻ precursor was prepared by mixing 0.5 mol/L zinc acetate dihydrate (Zn(CH₃COO)₂·2H₂O) and 5M NaOH (volume ratio, v/v 1:1, pH~14). The preparation of ZnO with different morphologies such as marigold-flower like (MGFL), multipod-jasmine-flower like (MPJF), urchin-rod-flower like (URFL), calendula-flower like (CDFL) and rice-grain-shape like (RGSL) morphologies are synthesized by microwave hydrothermal (MW-HT) and solvothermal (MW-ST) process illustrated in

Figure-1 employing the Anton-Paar (Multiwave PRO) microwave reaction system SOLV. First either $[\text{Zn}(\text{NH}_3)_4]^{2+}$ or $[\text{Zn}(\text{OH})_4]^{2-}$ precursor solution was mixed with different solvents such as water, ethanol, ethylene glycol and with and without zinc metal powder in a quartz vessels then positioned on a turnable stage for uniform heating in an Anton-Paar (Multiwave PRO) microwave reaction system SOLV. The microwave exposure time varying with respect to time and temperature was programmed with the Anton Paar Multiwave Pro software. The automatic pressure and temperature controls system allowed incessant monitoring and control of the interior temperature ($\pm 1^\circ\text{C}$). The preset profile (time, temperature, pressure) was followed automatically altering the applied power (0- 900 W) and the pressure upto 80 bar). The operating frequency of the system is 2.45GHz under hydro-/solvothermal condition. After MW-HT/ST reactions were over, the reaction vessels were cooled using inbuilt fast cooling fan system to room temperature. The white precipitate of ZnO deposited at the bottom of the quartz vessel that was filtered and washed more than a five times with distilled water, followed by absolute ethanol. Finally, the white ZnO were collected by centrifugation and the obtained precipitate was dried in vacuum at 60-70°C. The MW-HT/ST reaction parameters for each experimental series were summarized in Table S2 (Supporting information).

XRD characterization of the samples were carried with a Rigaku Ultima IV X-ray diffractometer with Cu K α radiation ($\lambda = 1.54 \text{ \AA}$) produced at 40 kV and 30 mA to scan the diffraction angles from 20-80°. Phase identification was made using standard ICDD (International centre for diffraction data) for the obtained products. The morphology of the samples was observed with field emission scanning electron microscope (FESEM-SUPRA-55)-Carlzeiss, Germany, while transmission electron microscopy (TEM) images and selected-area electron diffraction (SAED) patterns were taken with a JEOL 3010. Raman and Room-temperature photoluminescence spectra were recorded with Renishaw in Via system using excitation energy of a 514 nm laser and Fluoromax Spectrofluorometer (Horiba) respectively. The diffused reflection spectra (DRS) of ZnO were measured by a UV-visible spectrophotometer (UV-2550, Shimadzu, Japan). The specific surface area and average pore volume (Brunauer-Emmett-Teller, BET) were measured by using a micromeritics Gemini VII 2390 series. Photovoltaic (PV) measurements were performed using a Newport® 150 W 96000 solar simulator set at 100 mW cm⁻² full spectrum power using AM1.5G filter. The photocurrent density-voltage (J-V) curves were produced using a Keithley 2400 source meter. By using a standard silicon photodiode, the light intensity of the xenon light source had been calibrated. Electrochemical Impedance spectroscopy (EIS) was measured by a Biologic potentiostat-galvanostat (SP-150) under open circuit (V_{oc}) under illumination. The frequency ranges from 0.1 Hz to 10⁵ Hz with magnitude of the alternative (AC) signal was of 10 mV.

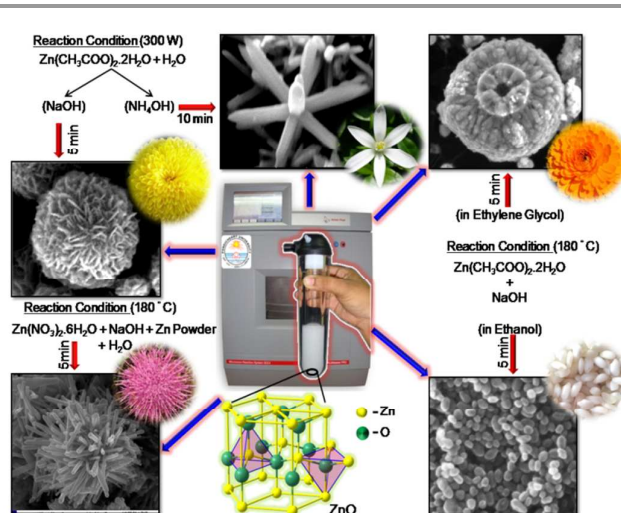


Figure 1. Schematic representation of different hierarchical marigold-flower like (MGFL), multipod-jasmine-flower like (MPJF), sea urchin-rod-flower like (URFL), calendula-flower like (CDFL) and rice-grain-shape like (RGSL) morphologies of ZnO synthesized by facile and rapid MW-HT/ST controlled heterogeneous nucleation process by decomposing $[\text{Zn}(\text{OH})_4]^{2-}$ and $[\text{Zn}(\text{NH}_3)_4]^{2+}$ precursor in various solvents without requiring any organic structure-directing agents or templates.

DSSC device fabrication and Physical Characterization

0.5 g of the prepared ZnO sample was dispersed into 4mL ethanol by ultrasonication for 10 minutes. Then 1.5 g terpeneol and 0.10 g ethyl cellulose were added and the solution was again ultrasonicated to form a homogenous viscous paste. The prepared paste was deposited on cleaned fluorine-doped tin oxide (FTO) glass substrate (transparent electrode present typical square sheet resistance of 10 Ω/sq and overall transmittance about 85% in the visible range) by doctor blade method to get a thickness of $\sim 17 - 23 \mu\text{m}$ using 3M scotch tape into an area of 0.25 cm² (with proper masking). After drying in air the coated substrates were heated in a furnace (400°C for 30 minutes). After attaining room temperature, substrates were then immersed in 0.5mM solution of N719 dye (Sigma-Aldrich) solution for 30 minutes (minimum sensitization time is used to avoid the dye-Zn²⁺ complex formation). Eight ZnO nanohybrid based DSSCs devices were made from four different MGFL, MPJF, URFL, and CDFL like ZnO flower like morphologies with different mass ratio of 5, 20, 50, and 80 wt% mixed with rice grain shape like ZnO (RGSL) by using a mortar and pestle to form a paste. The mixed hybrid samples were subsequently dispersed in ethanol and fabricated the photoanode as explained above.

To be specific, mixed RGSL/URFL hybrid photoanodes were blended in nanoscale level and subsequently fabricated by doctor-blade technique. We adopted the same doctor-blade technique to prepare the double layered ZnO photoanodes-based DSSCs. To be specific, after one layer of ZnO film coated on the FTO glass by using doctor blade, the wet film was then exposed to air for 15 min and then kept inside the drying oven

at 80°C for 15 min. After that, second layer was coated on top of first layer. The first double layered DSSC device was fabricated by RGSL as an under layer after the film was dried in room temperature, on top of it URFL layer was coated. The second double layered DSSC device was fabricated vice-versa as explained above. The double layered photoanode obtained as such was dried in room temperature and then sintered at 400°C for 30 minutes and subsequently soaked in dye solution as explained above. The Pt-counter electrode was fabricated by drop casting 5mM H₂PtCl₆ solution on to FTO and sintered at 400°C for 20 min. The two electrodes were sandwiched together with surlyn film of 30µm thickness as spacer. The redox couple electrolyte consisting of 0.06M 1-butyl-3-methyl imidazolium iodide, 0.03M of iodine solution (I₂), 0.10M guanidinium thiocyanate, 0.5M 4-tert-butylpyridine in a mixed solvent of acetonitrile and valeronitrile (volume ratio, 85:15) was introduced into the DSSC. The absorbed N719 dye quantity for all ZnO photoanode can be measured by UV-Visible absorption spectra of solutions containing dye desorbed from the ZnO film. The dye desorption studies were conducted by dye loaded photoanodes placed in 3mL of 0.1M of NaOH in mixed solvent of water /ethanol (v/v ratio 1:1) solution, and the UV-Visible absorption spectrum of the resultant solution was measured to estimate the adsorbed amount of dye. 0.5mM dye was dissolved in 0.1M NaOH as a reference. Ultimately, the dye was completely desorbed from the photoanode, the amount of dye molecules absorbed were calculated according to the Beer - Lambert's law

$$A = \epsilon \cdot c \cdot l$$

Where 'A' is the absorbance, $\epsilon = 8.176 / M \text{ cm}$ is the maximum molar extinction coefficient of the dye at 500 nm and 'l' is the path length of the light and c is the concentration of the dye.

RESULTS AND DISCUSSION

Structure and Morphology of ZnO

X-ray Diffraction analysis:

XRD patterns of different morphologies of hierarchical ZnO prepared via MW-HT and MW-ST controlled heterogeneous nucleation process by decomposing Zn(OH)₄²⁻ and Zn(NH₃)₄²⁺ precursor within 20 mins at temperature from 70 - 180°C, with microwave power of 300 - 900 W in various polar solvents such as H₂O, ethylene glycol, and ethanol without requiring any organic structure directing agents or templates, are shown in figure 2a – e. Significantly, all synthesized ZnO powders are of hexagonal phase with wurtzite structure belonging to space group P6₃mc. The XRD patterns of ZnO with different morphologies (Figure 2a - e) denote that all the diffraction peaks are well matched to hexagonal phase ZnO diffraction peaks with lattice constants a=0.3249 Å and c=0.5207 Å which is consistent with the reported values in JCPDS card (No.36-1451).

The diffraction peaks clearly show no other impurities, thus suggesting the product has high purity and wurtzite structure. In addition, peak broadening which appears from the

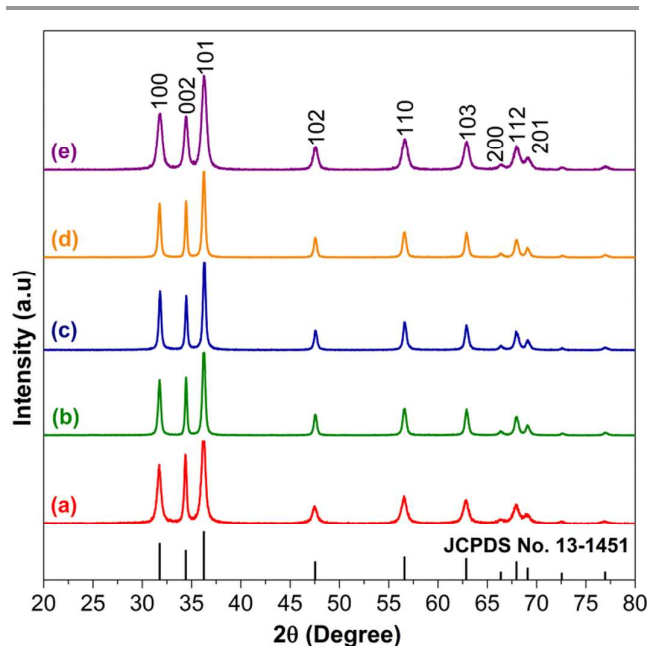


Figure 2. XRD patterns showing Different hierarchical ZnO morphologies of (a) MGFL, (b) MPJF, (c) URFL, (d) CDLF and (e) RGSL synthesized by MW-HT/ST controlled heterogeneous nucleation process by decomposing Zn(OH)₄²⁻ and Zn(NH₃)₄²⁺ precursor within 10 min at 70 - 180°C, microwave power of 300 - 900W in various solvents.

diffraction pattern is attributed to the fact that the obtained ZnO is small crystallite in size. During the preparation of precursor solutions by mixing Zn²⁺ ion with NH₄OH and NaOH such as [Zn(NH₃)₄]²⁺ and [Zn(OH)₄]²⁻, the Zn²⁺ ions are introduced into the OH⁻ aqueous solution. When ammonium hydroxide (NH₄OH) was introduced into the reaction solution, the lone-pair of electrons from nitrogen coordinate with the empty orbitals of Zn²⁺ ions that could generate metal-ammonium complexes such as [Zn(NH₃)₄]²⁺. On the other hand, when NaOH was introduced into the reaction system [Zn(OH)₄]²⁻ complex was formed.³⁷ The soluble Zn(OH)₄²⁻ precursor in H₂O solvent decomposes at MW-HT reaction. It is noticeable that the (002) planes of MPJF, MGFL and URFL synthesized products were extremely strong in comparison with standard JCPDS data, revealing the oriented growth of these hierarchical structures along (001) plane or c-axis direction.³⁸ Interestingly, the oriented growth along c-axis is substantiated by calculating the full width half-maximum (FWHM) of (002) peak which is narrowest when compared to the other peaks.³⁹

The significant difference in the FWHM supports our implication that ZnO crystals may lead to growth along the (001) plane (Table S1, in the supporting information), resulting in the formation of nano-rods/nano-petals and aggregates that served as the substrates to promote flower-like ZnO secondary heterogeneous nucleation. The phase structure and crystalline nature of ZnO play an important role in the PV conversion efficiency of DSSC after hybridization of two different flowers and rice grain like nanoparticle morphologies photoanode film coated on FTO substrate. Figure S1 (Supporting information) illustrates the XRD patterns of the ZnO film photoanodes with

different components and FTO glass substrate. Apparently, six peaks attributed to SnO_2 were observed for all XRD patterns. It is clearly revealed that all four hybrid photoanodes such as MGFL/RGSL, MPJF/RGSL, URFL/RGSL and CDFL/RGSL diffraction peaks illustrated the identical diffraction peaks of the powder samples despite minor differences in intensities of the peaks and can be exactly indexed to wurtzite ZnO structure with hexagonal phase (JCPDS no. 36-1451) and also indicating that the film was free from cracks and defects.

FE-SEM & TEM Studies of ZnO

The morphology and size of the as-synthesized ZnO crystals are further characterized by FE-SEM. The summarized reaction conditions and morphologies are provided in Table S2 (Supporting Information). Figure 3 shows the FE-SEM images of spectacular hierarchical nano-flowers and rice-like granular network morphology of ZnO at lower and higher magnifications. SEM images of all samples revealed flower like morphology that gives jasmine, marigold, urchin, calendula-like impression as shown in Figure 3 a - h.

In contrast, Figure 3 i, j shows a network of granular rice grain like structures (RGSL). When viewed closely at higher magnifications, MPJF and URFL are found to have microrod like petals making up of the flower with more *c*-axis growth as discussed earlier in XRD. In the case of MPJF, the micro-rods have length of 2 – 3 μm and diameter of about 100 – 500 nm (Figure 3d), while URFL consists of nanorod like morphology with a diameter of 10 – 60 nm and length of 300 – 600 nm with high magnified images which are shown in Figure S3 b, c in the supporting information and most of which have been aligned together into flower-like structure. It is also observed that the hierarchical MGFL flowers with diameter of 10–40 μm are randomly aggregated into nanosize petals of 25 - 45 nm with porous structures (Figure S3,a) but giving an overall morphological look of a spherical shaped marigold like structure as shown in Figure 3 a, b.

We found that the as-synthesized hierarchical flower like morphologies have further advantages that the microstructures are strong enough to undergo ultrasonic treatment, indicating the presence of strong structural interaction among the nanorods and nanoflakes. Typically, ZnO crystal growth is influenced by the internal and external factors such as intermolecular bonding preferences and other reaction parameters (precursor, nature of solvent, temperature, time and autogenous-pressure developed inside the MW-reaction vessel) respectively. The most stable wurtzite ZnO is a polar crystal which consists of O^{2-} ions in a hexagonal close-packed (HCP) arrangement, with each Zn^{2+} laying within a tetrahedral group of four oxygen ions as shown in Figure 1.

Zinc and oxygen atoms are arranged alternatively along the *c*-axis, demonstrating that the Zn^{2+} -terminated ZnO (0001) polar plane is chemically active, however the O^{2-} -terminated negative (1000) polar plane is inert. Compared with other crystal planes, the velocities for growth under MW-HT conditions are reported to be (0001) > (0110) > (1000). Eventually, the (0001) polar plane ZnO crystal has higher

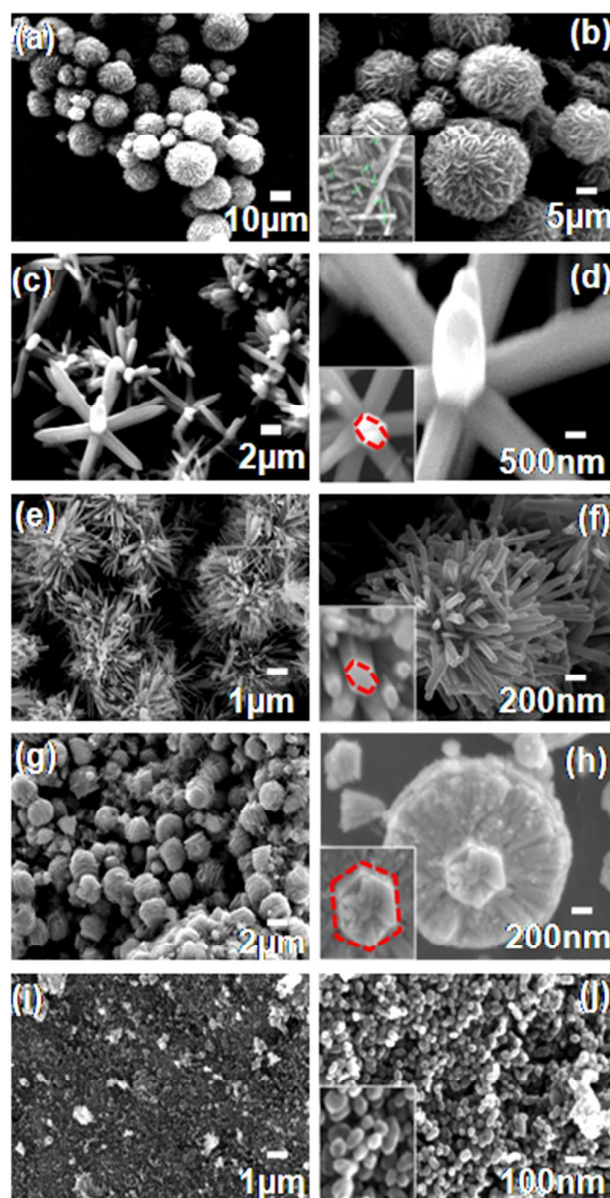


Figure 3. FESEM images of hierarchical ZnO flowers at different magnifications (a, b) for MGFL, (c, d) MPJF, (e, f) URFL, (g, h) CDFL, (i, j) RGSL, prepared by MW-HT/ST methods

surface energy and faster growth rate and thus the inherent asymmetry along the *c*-axis promotes the epitaxial crystal growth along the 0001 plane of 1D ZnO nanorods.⁴⁰

Hence our results are consistent with all the flower-like morphologies of ZnO which illustrate the preferential growth along the *c*-axis as shown in Figure 3 a - f. While, decomposing soluble $\text{Zn}(\text{OH})_4^{2-}$ in ethylene glycol (EG) *via* MW-ST condition, calendula-flowerlike (CDFL) morphology was obtained and shown in Figure 3 g, h. The growth mechanism of the CDFL-ZnO geometrical shape appears due to the nucleation and epitaxial growth on the central bigger-rod core which was surrounded by side branched nanorods of the central core (1010). We found that the OH^- ion concentration in the EG

reaction solution is playing an important role by influencing the different crystal faces and controlling the growth rate of anisotropic ZnO crystal formation. In contrast, when we decompose soluble $\text{Zn}(\text{OH})_4^{2-}$ in ethanol (EtOH) under MW-ST condition, the “rice grain” like morphology of ZnO was formed and its shape appears almost like rice grain with spheroid body like ZnO nanoparticles with diameter of 20 - 40 nm as shown in Figure 3 i, j and in supporting information Figure S3,d. Thus, MW-HT and MW-ST methods offer attractive routes for synthesizing different morphologies of ZnO materials.

TEM and HRTEM analysis were performed for the further understanding of crystal structure and morphology of ZnO. Figure 4 shows the typical TEM images of a number of individual ZnO micro-/nanorods grown in solution without any surfactant or hard templates. Figure 4 c, f, and i also exhibits lattice fringes corresponding to the ZnO lattice relating to ‘d’ spacing value of 0.28 nm between two lattice fringes corresponding to the (100) planes of ZnO hexagonal phase and also demonstrating the crystalline nature of the flower-like ZnO consisting of many nanorods and petals. Crystalline nature of ZnO was also confirmed by selected-area electron diffraction (SAED) as illustrated in Figure 4 b, e and h, which reveals a diffraction ring pattern corresponding to the wurtzite-structured crystalline ZnO.

From these FESEM and TEM images we can attribute that the hierarchical arrangements of the samples were able to provide higher surface area by forming different layers as well as macro to nano-porous structures, which is more desirable for high dye loading and also for better diffusion of electrolyte for DSSC.

Growth process of hierarchical ZnO in MW-HT/ST conditions

In our MW-HT/ST experiments there are five different parameters such as polarity of solvents, temperature, time, microwave power and kinetic energy barrier that can influence the crystal growth patterns under non-equilibrium kinetic growth conditions of different ZnO morphologies formation in the microwave assisted solution based approach. Indeed, microwave irradiation induces heating by the mechanisms of dipolar polarization and ionic conduction. Whereas the dipoles in the reaction mixture (for example, polar solvents such as H_2O , EG and EtOH) are involved in the dipolar polarization effect, the charged particles in a sample (Zn^{2+} ions) contribute to ionic conduction. When irradiated at microwave frequencies, the dipoles or Zn^{2+} ions of the sample align in the applied electric field. As the applied field oscillates, the dipole or ion field attempts to realign itself with the alternating electric field and, in the process, energy is lost in the form of heat through molecular friction and dielectric loss. Electric field present leads to orientation effects of dipolar molecules and then lower the activation energy according to the Arrhenius equation.³⁴ Lower activation energy leads to rapid nucleation and growth of the reaction mixture.³⁴ Either in aqueous or non-aqueous solution, the growth of ZnO crystals is usually divided into two stages, nucleation followed by growth processes. Noteworthy to mention here, during the

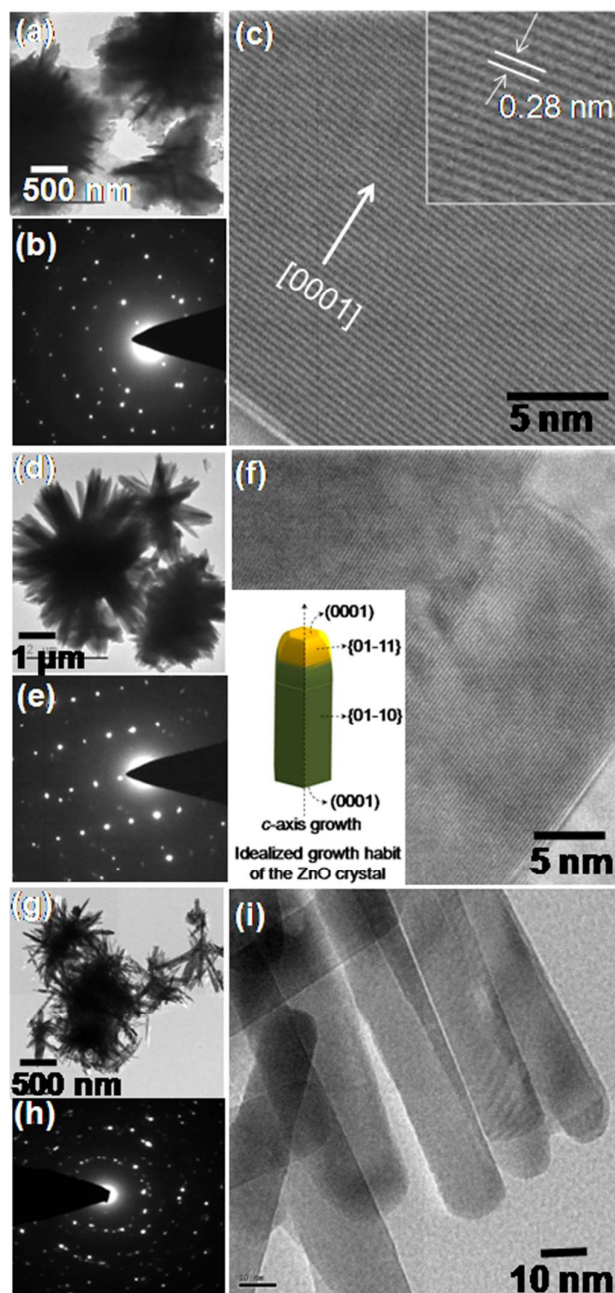


Figure 4. HR-TEM images and SAED patterns of hierarchical ZnO nanoflowers at different magnifications (a - c) for MgFL, (d - f) for MPJF and inset figure show the crystal growth direction along the c-axes, and (g - i) for URFL are prepared by MW-HT/ST methods

nucleation process the initial seeds formed are shape-determinant for the formation of final secondary growth flower-like ZnO structure.

The primary structures of ZnO are formed with many crystalline boundaries and more defects, thus rendering them thermodynamically unstable and kinetically favoured. With the rapid and uniform heating using the microwave synthesizer, the as-formed primary aggregates undergo oriented growth mechanism resulting in numerous oriented ZnO

nanoclusters.^{37,41} The oriented attachment of ZnO nanoclusters could effectively decrease the total surface energy of the system, which facilitates the fusion of adjacent ZnO clusters. Since the hexagonal ZnO having the anisotropic character, the nanoclusters formed would rearrange themselves get orientally attached along the *c*-axis in the case of nanorod like flower morphologies.^{42,43} Such *c*-axis preferential growth is evident from XRD, FESEM and TEM images.

Growth mechanism of CDFL-ZnO in EG and RGSL-ZnO in EtOH

When growth mechanism of CDFL-ZnO in ethylene glycol (EG), Zn²⁺ ions in Zn(CH₃COO)₂ could react with the EG molecules to form coordination complexes such as EG(Zn)²⁺, most probably depending on the concentration of EG.⁴⁴ At elevated temperature (180°C) and pressure the EG(Zn)²⁺ complexes dissociated to produce ZnO seed crystals in the presence of dissolved oxygen in the solvent. These as-synthesized ZnO seeds guided by the crystal symmetry agglomerated together to form a hexagonal planer nucleus. As the microwave solvothermal reaction continues the resulting structures experiences attachment process due to the strong capping ability of EG.⁴⁴ The surface energy of the individual hexagonal structures are quite high due to the more exposed planar surfaces and thus the formed structures are subject to fuse to each other and finally leads to the formation of rotor-shaped ZnO microstructures. Usually, hierarchical ZnO microstructure possess negative polar plane is rich in oxygen and positive polar plane is rich in Zn. Hence, the positive polar plane (0001) is being the more reactive subsequently it can attract new ZnO species to its surface. Generally, a ZnO with the (0001) growth plane bound by six facets is formed.

On the other hand growth mechanism of rice-grain shape like (RGSL) ZnO nanoparticles in ethanol were formed from zinc acetate dihydrate under the basic condition provided by NaOH. The growth process occurs through the formation of tetrahydrozincate, [Zn(OH)₄]²⁻. Since the Zinc acetate dihydrate concentration is very low compared to the NaOH concentration, which accelerates the self-assembly of sphere-like ZnO rather than rod/flower-like ZnO.

Growth mechanism of MGFL, MPJF and URFL ZnO in H₂O

While the reaction was carried out in H₂O, the reaction precursor gets dissolved homogeneously than in EG and EtOH, and subsequently the growth of the crystal nucleus is subjected to less confinement in a boiling droplet of solvent as reported by Zhang *et al.*⁴³ Therefore, it is responsible to form a spectacular marigold (MGFL) and jasmine (MPJF) flowers like morphologies in H₂O rather than rotor-like (CDFL) in ethylene glycol and sphere rice-like RGSL-ZnO morphology in ethanol respectively. In addition, the orientation growth of the ZnO is more comprehensible in water and the size is slightly larger.

The effects of pH and reaction temperature are important reaction parameters for obtaining different morphologies of ZnO under microwave-hydrothermal reaction condition. While NaOH is being added into Zn²⁺ solution, the high reactant

concentration led to the burst of initial homogenous nucleation and the supersaturated ZnO nuclei have been aggregated together. When the microwave reaction precedes the concentration of the ZnO₂²⁻ monomer became less, and active sites on the surface of initially formed ZnO aggregate able to grow along the oriented direction as long as the reaction medium in the quartz vessel provides reactants. The preferential growth plane along 0001 and (01 $\bar{1}$ 0) directions within the (21 $\bar{1}$ 0) plane formed nanosheets on the initial ZnO nuclei. Subsequently, several nanosheets with (21 $\bar{1}$ 0) plane surface intertwined and overlapped to each other into a multilayered secondary microstructured marigold flower like (MGFL) morphology of ZnO would formed. Further these results also supported by Li *et al* recently reported growth mechanism of flower like ZnO microstructure.⁴⁵

To explain the growth process of the sea-urchin like ZnO nanostructure, when metallic zinc powders are first melted and aggregated to form micro-sized Zn-droplets combine along with Zn(NO₃)₂ and Zn(OH)₂ under MW-HT condition at high temperature of 180°C to form nanosize ZnO nuclei. The nuclei thus play a crucial role in the growth of ZnO nanowires, which grow till the Zn source is almost used up. So from each zinc droplet there is an origination of several ZnO nanorods which lead to the formation of sea urchin-like structure. Here the zinc metal powder plays a key role for the nanorod formation, which is capable to accelerate further nucleation and the growth process besides the high reaction temperature lead into the formation of URFL-ZnO morphology. The grown nanorods are highly crystalline nature with preferred orientation along (0001) plane, and shows that the lattice fringes are spaced 0.28 nm. When ammonia is used as the hydroxide generating agent, Zn²⁺ ions readily react with hydroxide anions to form a stable tetrahedral complex [Zn(OH)₄]²⁻. Other than [Zn(OH)₄]²⁻ ammonia can also provide [Zn(NH₃)₄]²⁺ complex thus generates more growth units around ZnO nuclei leading to faster growth kinetics. Moreover ZnO can easily form multipod structures consisting of several rods united at common base, large number of available growth units ([Zn(OH)₄]²⁻ and [Zn(NH₃)₄]²⁺) and faster growth kinetics leads to the formation of jasmine flower shape like ZnO due to the preferential growth along 0001 plane.

Hence, the solvents H₂O, ethylene glycol, and ethanol enable a smooth control to achieve the fractal patterns as different flowers and spherical rice like morphologies, shown in Figure. 3.⁴³ Due to the lower saturated vapor pressure and high boiling point of EG used in MW-ST reaction, the amalgamation of the nucleus becomes less intense compared to the lower boiling point and higher saturated vapor pressure of H₂O used in the MW-HT reaction. MW-HT/ST methods are effective to achieve different morphologies of ZnO adequately crystallized at relatively low temperatures (50 – 125°C) without requiring further calcinations at high temperatures. In this synthesis strategy, we obtained ZnO rods from Zn(OH)₂ precipitate by a hydrothermal process first, and then produced the calendula-flower like ZnO by using EG as a solvent, whereas spherical particle “rice grain” shaped ZnO was

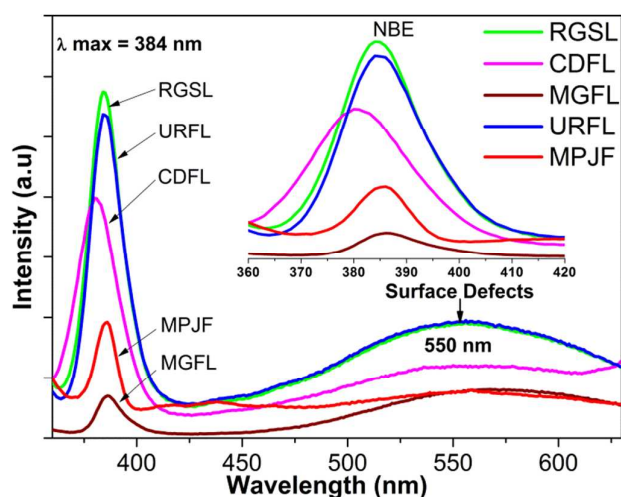


Figure 5. Room temperature photoluminescence (PL) spectra of various morphologies of hierarchical ZnO flowers (RGSL, CDFL, MGFL, URFL and MPJF) are prepared by MW-HT/ST methods, inset figure showing the UV near band edge emissions (NBE). The excitation wavelength was used for all samples is 340 nm.

obtained by using EtOH as solvent saturated with $[\text{Zn}(\text{OH})_4]^{2-}$ ions through epitaxial growth under solvothermal conditions.

Raman spectroscopy and optical properties of ZnO

To understand the molecular vibrational properties of MW-HT/ST synthesized ZnO crystals, we carried out the Raman spectroscopy analysis. Figure S2 (Supporting information) a-i represents the Raman spectra of individual flower like ZnO and hybrid ZnO photoanodes which have hexagonal wurtzite structure and belong to the C_{12h} ($P6_3mc$) space group with two formula unit primitive cell where all atoms occupy the C_{3v} sites. The presence of the Raman active modes for ZnO such as $A_1+2E_2+E_1$ is predicted by group theory⁴³ where A_1 and E_1 are infrared-active and can be split into transverse optical (TO) and longitudinal optical (LO) components. E_2 is only Raman active and nonpolar which consists of two modes with a low and high frequencies. For all samples four vibrations were detected which located at 333, 386, 439, 587 cm^{-1} . The sharp and major peak at 439 cm^{-1} (E_2) is attributed to the hexagonal wurtzite ZnO.⁴³ The high intensity and sharpness of the E_2 peak demonstrates the formation of hexagonal wurtzite phase with good crystallinity which was observed in the individual ZnO and hybrid ZnO. The small vibration peak at 333 cm^{-1} belongs to the second-order Raman scattering that originates from multiphonon process ($2E_2$). The peaks at 386 and 585 cm^{-1} correspond to the polar transverse (A_1) and longitudinal (E_1) optical phonon mode respectively.⁴⁵ The origin of E_1 peaks in the spectra caused by the development of defects in the structure such as oxygen vacancies and zinc interstitials. Compared to the E_2 mode, the intensity of E_1 mode is much lower, explaining the formation of wurtzite hexagonal ZnO phase of good crystal quality with less structural defects and impurities. We also observed that, all the characterized peaks

belonging to the individual ZnO are matching with hybrid ZnO photoanodes, except the peak intensities that are varied between them that are shown in Figure S2 (Supporting information)

We also examined how different morphologies could influence the photoluminescence (PL) properties of ZnO prepared by MW-HT/ST methods. The PL spectra of ZnO show different features, depending on their morphological variations and the spectrum were obtained with excitation wavelength of 340 nm as shown in the Figure 5. The obtained spectrum exhibits two bands, one is in ultraviolet emission (UV) peak at 384 nm (3.23 eV) and another weak and broad green-yellow emission peak at 550 nm (2.25 eV). We observed that defect emission in visible region is detected owing to the poor crystallinity of the nanostructured ZnO (particularly for MGFL and MPJF sample) which is caused by quenching.⁴³ The UV peak is attributed to the near band-edge emission (NBE) from the recombination of free excitons through an exciton-exciton collision process. The band emission at 550 nm recognized as deep level emission (DPE) has been belonging to impurities and structural defects exhibited by green emission (singly ionized oxygen vacancies) or yellow emission due to interstitial oxygen ions that originate from the radiative recombination of a photon-generated hole with an electron occupying oxygen vacancy. Devi *et al* recently reported the PL intensities of the ZnO are strongly depends on the crystallinity and surface defects formation upon increasing in the annealing temperature.⁴⁶ We found that, MGFL and MPJF samples exhibits very low PL peak intensities compare to RGSL, URFL, and CDFL because both of these samples are prepared at low temperature $\sim 90^\circ\text{C}$. Whereas, other three samples URFL, CDFL, and RGSL show higher PL peak intensities, is due to these three samples are prepared at higher MW-HT/ST reaction temperature of 180°C .

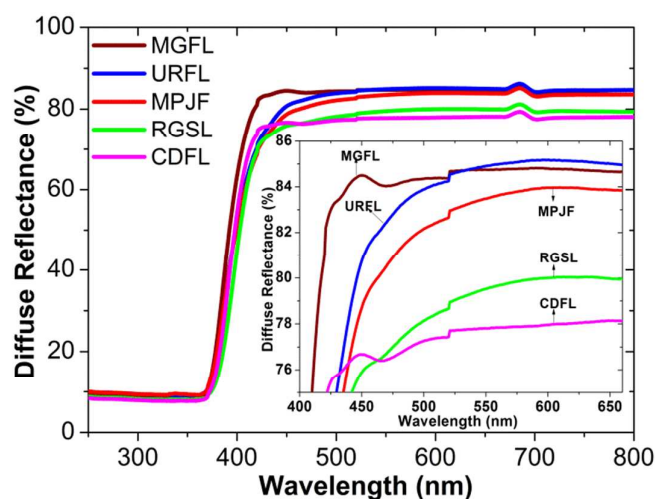


Figure 6. Diffuse reflectance spectra (DRS) of various ZnO morphology (MGFL, MPJF, URFL, RGSL and CDFL) prepared by MW-HT/ST methods, showing more than 80% reflectance

ARTICLE

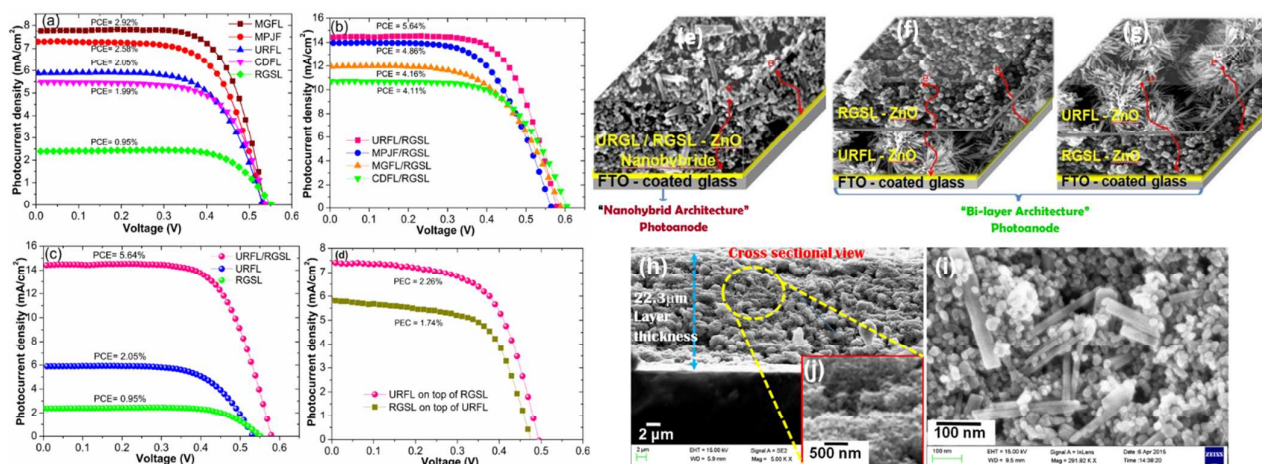


Figure 7. A comparative plot of J - V curves behaviour of DSSCs fabricated with photoanode made of (a) various morphologies of ZnO (MGFL, MPJF, URFL, RGSL and CDFL), (b) “nanohybrid architecture” made up MGFL/RGSL, MPJF/RGSL, URFL/RGSL and CDFL/RGSL (c) a comparative plot of URFL, RGSL, and URFL/RGSL hybrid structure (d) “bi-layer architecture” of URFL on top of RGSL and RGSL on top of URFL (e) schematic representation of “nanohybrid architecture” of URFL/RGSL-ZnO based DSSC and (f, g) schematic representation of “bi-layer architecture” of RGSL on top of URFL and URFL on top of RGSL based DSSCs. (h) Cross-sectional FE-SEM image of URFL/RGSL-ZnO nanohybrid photoanode architecture of film as well as magnified FE-SEM image of URFL/RGSL-ZnO hybrid layer and (i) Top-view of URFL/RGSL film clearly showing integrated URFL and RGSL-ZnO hybrid architecture.

These results also substantiate with XRD peaks intensity of URFL, CDFL, and RGSL samples are higher compared to MGFL and MPJF shown in Figure 2. Rai et al recently observed there has been blue shift in the PL emission of ZnO with respect to small size effect.⁴⁷ Indeed, we also observed the blue shift in the UV emission of RGSL and CDFL ZnO is owing to the smaller in size as compared to other morphologies, as the overall particle size calculated using Scherrer’s formula for RGSL (18.4 nm) and CDFL (14.6 nm) that is smaller than secondary microstructured MGFL (52.1 nm), MPJF (57.9 nm) and URFL (70.5 nm).

In order to examine the light-scattering property of the various morphologies of ZnO synthesized by MW-HT/ST methods, UV-Visible diffused reflectance spectra (DRS) were recorded and shown in Figure 6. We found that all ZnO samples are relatively inducing a strong scattering effect according to the Mie theory. As illustrated in Figure 6, the incident light passes through ZnO samples and then is significantly scattered and path length of incident light is extended, which results in an enhanced reflectance of more than 83% in the case of MGFL sample. In contrast, the reflectance of the MPJF and URFL samples showed the reflectance of 78% and 80% respectively and the reflectance values are not much different between them. We hypothesize that, the primarily formed nano-sheets and rods aggregated in

the secondary hierarchical flower like microstructures could induce the effective light scattering.

The strong scattering effect is exhibited from MGFL, MPJF and URFL samples, which is beneficial to the incident light harvesting and enhancement of PCE of the DSSCs. When compared to MGFL, MPJF and URFL samples, CDFL and RGSL samples are showed slightly lower reflectance that may be due to CDFL morphology in micron size. The small size of RGSL-ZnO nano-particles ranging from 10 to 25 nm that were relatively lesser than the wavelength of visible light, hence the nanoparticles was transparent with little light scattering. Moreover the band gap of the samples is determined from the Tauc plot Fig. S4 by plotting $(\alpha h\nu)^{1/2}$ vs $h\nu$, which is derived from the diffuse reflectance spectra. The obtained values are provided in the Fig. S4 (supporting information inset Table).

Photovoltaic characterization of DSSCs

Comparison of the PCE that is photocurrent density - voltage (J - V) curves of the DSSCs based on different hierarchical ZnO flowers, rice-grain like nanoparticles and their “nanohybrid architecture” as well as “bi-layer architecture” photoanodes are illustrated in Figure 7 and the corresponding photovoltaic parameters such as the open circuit photovoltage (V_{oc}), the short circuit photocurrent density (J_{sc}), the fill factor (FF), the overall energy conversion efficiency (η) and dye loading of the different photoanodes are summarized in Table

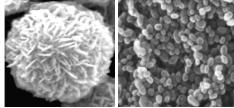
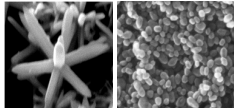
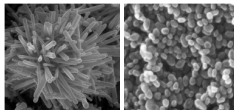
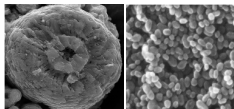
S3 (Supporting information) & Table 1. Interestingly, MGFL-ZnO photoanode showed an open circuit photovoltage (V_{oc}) of 538 mV, a fill factor of 70.2% and short circuit photocurrent density (J_{sc}) of 7.74 mA cm⁻² and representing overall conversion efficiency of 2.92%. However, MPJF-ZnO exhibits slight decrease in PEC of 2.58% and J_{sc} = 7.29 mA cm⁻² compared to MGFL-ZnO sample. URFL-ZnO and CDFL-ZnO samples are exhibits PCE of 2.05% and 1.99% respectively are shown in Figure 7a, however both sample shows comparable J_{sc} , V_{oc} and FF. In general, more photo-generated electrons and the photocurrent are sturdily related to the dye loading on the photoanodes. Therefore, the RGSL-ZnO based DSSC shows very low photocurrent density and low efficiency of 0.95%, however it exhibited improved voltage of 552 mV and FF of 71.2%. The result clearly exhibits a remarkable increase in conversion efficiency for hierarchical flower-like morphology compared to RGSL-ZnO sample, which may be ascribed to the more porous as well as open secondary microstructured hierarchical flower-like large particle size with enhanced light scattering properties. RGSL-ZnO sample showed relatively large fill factor (FF = 71.2%) because of the well interconnected granular structure which serve as an easy path for electron transport. However, they do not have sufficient photocurrent developed due to poor scattering ability. Thus, our results show that hierarchical ZnO flowers made up of dense packed primary oxide nanostructures (petals or rods) which can facilitate the electron transport throughout the ZnO film. Moreover, self-assembly of primary nanostructures are formed under MW/HT-ST condition followed by submicrometer scale secondary spherical flower structure which can generates effective light scattering since the particle size is comparable to wavelength of light. Innovatively, we have developed two types of photoanode configurations based DSSCs such as “nano-hybrid architecture” and “bi-layer architecture”. We made four different “nano-hybrid architecture” based DSSCs by hybridization of different types of flower-like ZnO with RGSL-ZnO nanoparticles such as URFL/RGSL, MPJF/RGSL, MGFL/RGSL, and CDFL/RGSL with PCE of 5.64, 4.86, 4.16, and 4.11% respectively as shown in Fig. 7b and the comparative PCE were obtained for all sample that is listed in Table S3 (supporting information). The enhanced efficiencies of all devices made of hybrid sample are attributed to the improved open circuit voltage (V_{oc}) and short circuit current density (J_{sc}). Among four nanohybrid architectures, URFL/RGSL based nanohybrid photoanode based DSSCs (Figure 7e) showed remarkably enhanced PCE of 5.64% which is higher than that of their individual components such as flower-like URFL-ZnO and RGSL-ZnO which exhibit PCEs of 2.05% and 0.95% respectively that are shown in Figure 7c. Moreover, high FF and increased J_{sc} are offered by a well-organized light scattering structure associated with efficient light scattering and higher dye loading that is related to larger surface area (22.26 m² g⁻¹) in URFL/RGSL-based nanohybrid device. In nano-hybrid architectures, the “size mismatching” of different flower morphological ZnO (such as MGFL, MPJF, URFL and CDFL) with rice-grain shape like ZnO (RGSL) offer too many open spaces with some macropores and mesopores between

ZnO flowers and nanoparticles of photoanode film. This well promotes the dye adsorption and efficient transport of electrolyte molecules. Our results obtained from the BET surface area analysis (Table S3 in supporting information) and dye loading measurements (Table S5 in supporting information) are well corroborating to each other. The improved dye loading of nano-hybrid samples facilitates more photo generated electrons and thus high J_{sc} compared to the individual morphological ZnO. The rice-grain shape like (RGSL) nanoparticle in nano-hybrid film offers better contact with FTO which improved the V_{oc} subsequently FF, can be understand from the photovoltaic performance data in Table S3 (supporting information). Our results also corroborated with Recently reported by Weng *et al* fabricated TiO₂ nanosheet/nanoparticle gradient films photoanode for DSSCs.⁴⁸ Thus, the performance of URFL/RGSL nanohybrid based DSSC as an example, for comparative purpose we also fabricated “bi-layer architecture” based DSSCs through layer-by-layer coating of flower-like URFL-ZnO on top of the RGSL-ZnO nanoparticles and *vice-versa* for making efficient DSSC as shown in Figure 7 f and g respectively. In contrast, two “bi-layer architecture” photoanodes were made up of RGSL-ZnO layer on top of the URFL-ZnO layer and URFL-ZnO layer on top of the RGSL-ZnO layer of DSSCs which exhibited PCEs of 1.74% and 2.26% respectively is shown in Figure 7 d.

It is revealed that the “hybrid architecture” exhibits superior enhancement in PCE compared to that “bi-layer architecture” assembly and their respective individual ZnO components. The bi-layer architecture is an inhomogeneous material and structure of two different morphologies of ZnO. The hybrid architecture enables the homogeneous photoanode film to have the best advantages of both URFL-ZnO and RGSL-ZnO in nanoscale as shown in Figure 7 i. The film thickness with coated layer estimated from Figure 7 h was about 22.3 μm and no obvious boundaries were 7b served between each coated layers that facilitate the low charge recombination rate and fast electron transfer between the URFL-ZnO and RGSL ZnO nanoparticles.

The enhancement in PCE in the “nano-hybrid architecture” was mainly attributed to the synergetic effect when two different morphologies are blended together at “nanoscale” level. URFL-ZnO nanorods may act as the bridges between nanocrystalline RGSL-ZnO aggregates to construct network interconnections within urchin-ZnO film and thus offer more pathways for electron transport. In addition, RGSL-ZnO nanoparticles facilitate the fast electron transport through better inter-particle and electronic contacts with fluorine-doped SnO₂ glass substrate. The comparative *J-V* curves of different morphologies of ZnO and their respective nanohybrids are illustrated in Figure S5 in the supporting information. Hence, our results provide a promising way to enhance the PCE in ZnO based DSSC. It has been reported that the dye anchoring with photoanode films was considerably determined by the PCE of DSSCs. We demonstrated dye desorption experiments that the amount of dye absorbed on the five films were obtained by measuring the UV-Visible absorption spectra of solutions containing dye desorbed from

Table 1: DSSC photovoltaic performance data determined by photocurrent density-voltage (*J*-*V*) characteristics analysis of different compositions of different hierarchical flowers like morphologies mixed with rice-grain shape like nanoparticles of ZnO hybrid nanostructure are prepared by MW-HT/ST methods

Sample code of ZnO Nanohybrids	Composition Wt. %	V_{oc} (mV)	J_{sc} (mA/cm ²)	FF	η (%)
MGFL-RGSL 	05:95	510	04.41	69.0	1.55
	20:80	559	06.52	73.3	2.67
	50:50	589	11.91	59.4	4.16
	80:20	602	08.57	55.8	2.88
MPJF-RGSL 	05:95	604	07.11	67.8	2.91
	20:80	564	13.96	61.7	4.86
	50:50	587	11.96	54.0	3.79
	80:20	593	12.60	53.4	4.00
URFL-RGSL 	05:95	566	11.68	62.6	4.13
	20:80	575	07.43	68.4	2.93
	50:50	579	14.33	68.0	5.64
	80:20	612	06.77	62.9	2.60
CDFL-RGSL 	05:95	503	09.73	62.5	3.06
	20:80	573	10.83	63.8	3.97
	50:50	629	08.39	61.4	3.24
	80:20	604	10.72	63.5	4.11

the films in NaOH aqueous solution. Figure 8a and b show the optical absorption containing N719 dye desorbed from different sensitized ZnO films fabricated using individual morphological component and hybrid of ZnO respectively. The amount of dye loading was determined by the molar extinction coefficient. It is observed that the dye loading on the film MGFL-ZnO ($6.35 \times 10^{-7} \text{ mol cm}^{-2}$) is higher than MPJF-ZnO, URFL-ZnO, CDFL-ZnO and RGSL-ZnO ($6.25 \times 10^{-7} \text{ mol cm}^{-2}$, $6.05 \times 10^{-7} \text{ mol cm}^{-2}$, $5.48 \times 10^{-7} \text{ mol cm}^{-2}$, and $5.25 \times 10^{-7} \text{ mol cm}^{-2}$) respectively as provided in Table S3 (Supporting Information) that is well in agreement with PCE of different flowers like morphologies, rice-grain like ZnO, nanohybrid architecture and bi-layer architecture of ZnO based DSSCs. The hybrid structure will offer substantial surface area ($20.18 \text{ m}^2 \text{ g}^{-1}$, $21.48 \text{ m}^2 \text{ g}^{-1}$, $22.26 \text{ m}^2 \text{ g}^{-1}$ and $19.70 \text{ m}^2 \text{ g}^{-1}$ for MGFL/RGSL, MPJF/RGSL, URFL/RGSL and CDFL/RGSL respectively) to absorb more dye molecules and better particle-particle interconnection by RGSL-ZnO nanoparticles. Typical N₂ adsorption-desorption isotherms of RGSL and URFL/RGSL nanohybrid sample is given in Figure S6 (supporting information). The surface area, pore volume and pore diameter obtained from BET surface area analysis for all hierarchical ZnO and nanohybrid samples are given in Table S5 (in the Supporting information). The results clearly shows the improved surface area for all nanohybrid samples compare to the individual hierarchical flower morphological sample.

Therefore the hybrid structured photoanode are characteristic with better dye loading rate and enhanced absorption of light in the range of 400 - 800 nm which maximizes the J_{sc} . More interconnection between the particles provided by the RGSL-ZnO helps to improve the V_{oc} and all these factors are contributing for the enhancement in efficiency for all the hybrid structured photoanodes. Moreover, the DRS data obtained is well correlated with the photovoltaic performance of the samples.

Electrochemical impedance spectroscopy (EIS) analysis

The electrochemical impedance spectroscopy (EIS) analysis has been carried out to further comprehend the effect of the film structure on the PV performance of DSSCs. EIS is regarded as a powerful technique for studying the electron transport and recombination process during the photovoltaic process of DSSCs.⁴⁹ EIS of DSSCs was carried out to investigate the difference in the interfacial characteristics of the ZnO based photoanodes under AM 1.5 illumination at applied potential bias of V_{oc} and frequency ranges from 10^{-1} Hz to 10^5 Hz with AC amplitude of 10 mV. Figure 9 a, b represents the EIS curves in

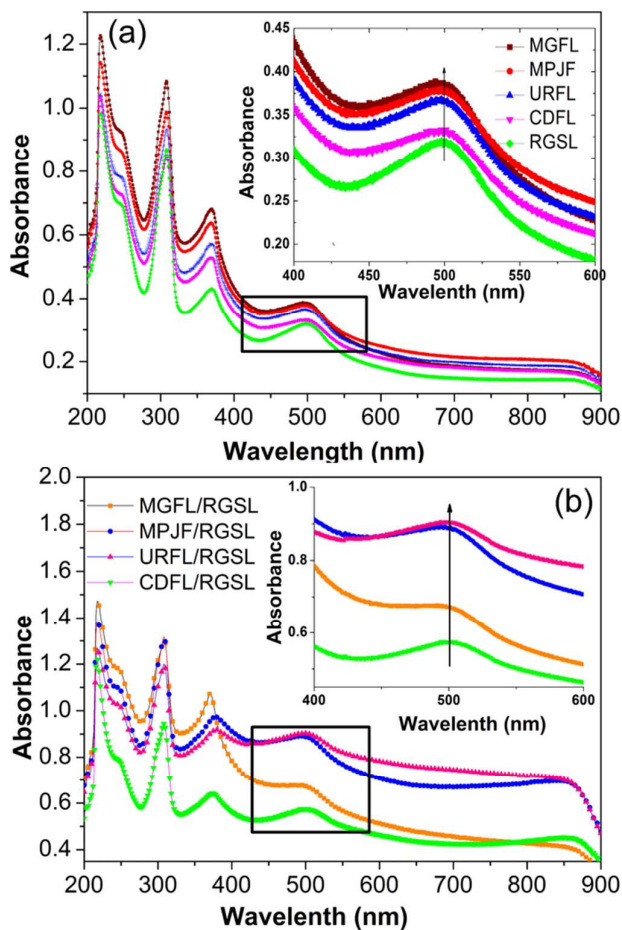


Figure 8. UV-Visible absorption spectra of N719 dye desorbed from different ZnO photoanode films of (a) MGFL, MPJF, URFL, CDFL and RGSL and (b) MGFL/RGSL, MPJF/RGSL, URFL/RGSL and CDFL/RGSL hybrids.

the form of the Nyquist plots and corresponding Bode phase plots. In the equivalent circuit (inset in Figure 9) generated by Z fit software fitting, the circuit elements contain series resistance R_s , internal resistance R and capacitance or constant phase element (CPE). The electron-dynamic parameters evaluated from the fitted Nyquist plots and Bode phase plots were summarized in Table S4 (See Supporting Information). In general the Nyquist plot shows three semi-circles at the high, middle, low frequency region or three characteristic frequency peaks in a Bode phase plot. The small semi-circle in the high frequency region corresponds to the redox and electron transfer reaction at the Pt counter electrode electrolyte interface. The middle frequency semi-circle is associated with charge transfer and electron recombination resistance and low frequency region is associated with the resistance provided for diffusion of ions in the electrolyte. Figure 9 illustrates the Nyquist plots of URFL/RGSL-ZnO nanohybrid photoanodes based DSSCs and their individual component such as URFL and RGSL respectively. The impedance components of the interfaces in DSSCs revealed in the frequency regions of 10^3 to 10^5 Hz, 1 to 10^3 Hz, and 10^{-1} to 1 Hz are related with the charge transport at the FTO/ZnO (R_s) and Pt counter electrode-electrolyte interfaces (R_1), the ZnO/dye/electrolyte interfaces (R_2), and the ionic diffusion in the electrolyte (Nernstian diffusion, R_3) respectively. The summarized results of EIS analysis is fitted by using an equivalent circuit containing capacitance and resistance (Figure 9) as shown in Table 4. In the main, the first gap (R_s) in Nyquist plot is related to the FTO sheet resistance and the contact resistance between FTO and ZnO. The middle frequency in the Nyquist plot is assigned to charge transport resistance and the charge recombination resistance of ZnO to tri-iodide in the electrolyte. However, under illumination, such as AM 1.5, the electron density in the conduction band of ZnO will be high, thus middle frequency is reduced to a simple arc that generated by the capacitance of ZnO paralleled with the charge recombination resistance. Thus the second semicircle represents the charge recombination resistance. The larger charge recombination resistance imply small recombination rate of photo injected electrons with tri-iodide, which is favourable to achieve high cell performance.

Among the three DSSCs devices such as URFL, RGSL and URFL/RGSL, the large semicircle at middle frequency for the URFL/RGSL device is the smallest and which indicates the hybrid architectures accelerated electron transfer in DSSC through reduction of charge transfer resistance leading to increase of the J_{sc} . Moreover the middle semicircle is larger compared to the first and third semi-circle, implies lowest hole-electron recombination which possibly due to the remarkable electron transport properties of nanorods assembly structure of URFL-ZnO.

Figure 9b shows the Bode phase plots generated using the impedance results. From the Bode plot, the lifetime of the photo-injected electrons (τ_e) in the URFL, RGSL and URFL/RGSL hybrid ZnO can be calculated from the peak frequency (f_{max}) in the middle frequency region according to the equation

$$\tau_e = 1/2\pi f_{max}$$

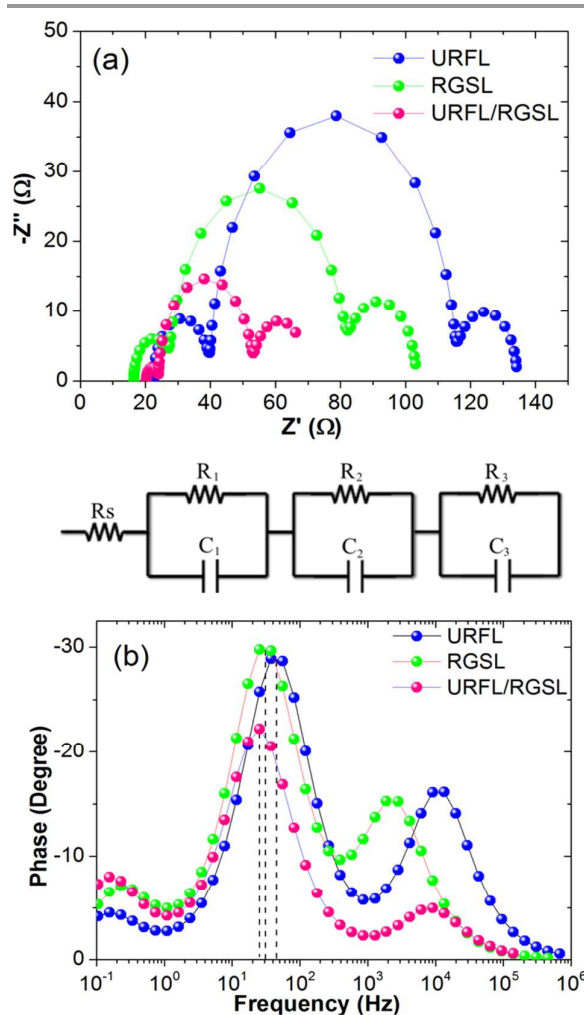


Figure 9. EIS spectra of URFL, RGSL, URFL/RGSL hierarchical ZnO hybrid photoanode based DSSCs (a) Nyquist-plots and (b) Bode phase-plot and equivalent circuit model.

Where f_{max} is the maximum characteristic peak frequency at the middle frequency region.

The electron life time (τ_e) value of DSSCs based on URFL, RGSL and URFL/RGSL hybrid photoanodes were calculated to be 3.4, 5.1 and 6.4 ms respectively. The longer τ_e means the lower recombination rate of electrons during the electron transfer across ZnO film.⁵⁰ Similar impedance results are reported for composite photoanode film of DSSCs by Puyoo *et al* and Wang *et al.*^{24, 48} Although the URFL/RGSL hybrid device had an τ_e slightly higher than that of URFL and RGSL device, it exhibits the highest J_{sc} and PCE among all possible devices that we made as shown in Table S3 (Supporting Information) and Table 1. Therefore, the strong light scattering ability with higher dye loading, and lower recombination of photo-injected electrons as well as effective electron transport were facilitated from URFL-ZnO that contributes to the highest photovoltaic efficiency of the URFL/RGSL hybrid DSSC.

Conclusions

In summary, we have fabricated different morphologies of ZnO by facile changing solvents and precursors without requiring any templates and surfactants via rapid MW-HT/MW-ST methods. MW-HT/ST condition induced “hot surface” on the ZnO nuclei speeding up the nanocrystal growth kinetics to make different forms of hierarchical structures of ZnO. It was observed that final morphologies are tuned mostly by highly anisotropic structure of ZnO as well as different polar solvents and precursor concentrations. Raman scattering and room temperature PL studies exhibited reliable results with respect to the crystallinity enhancement during MW-ST reactions. The enhanced conversion efficiency (5.64%) of the “nano-hybrid architecture” can be mainly attributed to “synergistic effects” of several factors, firstly in the URFL/RGSL-ZnO hybrid device, nanorods assembly of URFL morphology facilitate strong light-scattering effect that facilitates the incident light to be multi-reflected within the film, effectively extending the optical distance and improves light-harvesting and photocurrent density. Secondly, better electronic contact with the FTO glass was ensured by the nanoparticle assembly of RGSL morphology that could be provided the lower contact resistance and higher photovoltage. Thirdly, the nanohybrid architecture of URFL/RGSL-ZnO enables the homogeneous photoanode film to have the best advantages of both URFL-ZnO and RGSL-ZnO at nanoscale level and hybrid material by “size mismatched” URFL/RGSL combination can enhance the dye sorption, in contrast with inhomogeneous bi-layer architecture. This present investigation is intended to open up a new avenue for design and fabrication of novel DSSCs architecture with higher PCE. Finally, the facile, rapid and cost-effective MW-HT/ST methods can produce various oxides and sulfides in large-scale with controlled morphologies for clean energy conversion and storage device applications.

Acknowledgements

The authors express their gratitude towards the following funding agencies: University Grants Commission (UGC), Government of India, New Delhi under development of dye sensitized solar cells major project No. 41-376/2012, Pondicherry University Start-up grant No. PU/PC/Start-up Grant/2010-12/309 and DST-TSD grant No PT/2011/178-G for providing microwave synthesis facility in our lab. Ms. R. Krishnapriya specially thanks UGC for providing research fellowship. We also thank Central Instrumentation Facilities (CIF), Pondicherry University for materials characterization.

Notes and references

- 1 B. O'regan and M. Gratzel, *Nature*, 1991, 353, 737.
- 2 H. S. Jung and J.-K. Lee, *J. Phys. Chem. Lett.*, 2013, 4, 1682.
- 3 A. Hagfeldt, G. Boschloo, L. Sun, L. Kloo and H. Pettersson, *Chem. Rev.*, 2010, 110, 6595.
- 4 M-E. Ragoussi and T. Torress, *Chem. Commun.*, 2015, 51, 3957.

- 5 S. Mathew, A. Yella, P. Gao, R. Humphry-Baker, F. E. CurchodBasile, N. Ashari-Astani, I. Tavernelli, U. Rothlisberger, K. NazeeruddinMd and M. Gratzel, *Nat. Chem.*, 2014, 6, 242.
- 6 G. Cao and Q. Zhang, *Nano Today* 2011, 6, 91.
- 7 J. A. Anta, E. Guillen and R. Tena-Zaera, *J. Phys. Chem. C*, 2012, 116, 11413.
- 8 Q. Zhang, C. S. Dandeneau, X. Zhou and G. Cao, *Adv. Mater.*, 2009, 21, 4087.
- 9 K. Zhu, N. R. Neale, A. Miedaner and A. Frank. *NanoLett.* 2007, 7, 69.
- 10 Q. Zhang, D. Myers, J. Lan, S. A. Jenekhe and G. Cao. *Phys. Chem. Chem. Phys.* 2012, 14, 14982.
- 11 W. W. Sun, W. T. Peng, Y. M. Liu, W. J. Yu, K. Zhang, K. F. Mehnane, C. H. Bu, S. S. Guo and X. Z. Zhao, *ACS Appl. Mater. Interfaces*, 2014, 6, 9144.
- 12 Y. -Z. Zheng, X. Tao, Q. Hou, D. -T. Wang, W. -L. Zhou and J. -F. Chen, *Chem. Mater.*, 2011, 23, 3.
- 13 T. Ma, M. Akiyama, E. Abe and I. Imai, *NanoLett.*, 2005, 5, 2543.
- 14 J. Zhang, W. Peng, Z. Chen, H. Chen and L. Han, *J. Phys. Chem. C*, 2012, 116, 19182.
- 15 X. Zhang, F. Liu, Q. -L. Huang, G. Zhou and Z. -S. Wang, *J. Phys. Chem. C*, 2011, 115, 12665.
- 16 H. Xu, X. Chen, S. Ouyang, T. Kako and J. Ye, *J. Phys. Chem. C*, 2012, 116, 3833.
- 17 T. T. Chen, I. -C. Chang, M. -C. Tsai, Y. -C. Chang, M. -H. Yang, P. -C. Chen, H. -T. Chiu and C. -Y. Lee, *CrystEng Comm.* 2014, 16, 3341.
- 18 W. -Q. Wu, Y. -F. Xu, H. -S. Rao, C. -Y. Su and D. -B. Kuang, *J. Am. Chem. Soc.* 2014, 136, 6437.
- 19 R. Gao, Y. Cui, X. Liu, L. Wang and G. Cao, *J. Mater. Chem. A*, 2014, 2, 4765.
- 20 H. -L. Feng, W. -Q. Wu, H. -S. Rao, Q. Wan, L. -B. Li, D. -B. Kuang and C. -Y. Su, *ACS Appl. Mater. Interfaces*, 2015, 7, 5199.
- 21 Y. Bai, Z. Xing, H. Yu, Z. Li, R. Amal and L. Wang, *ACS Appl. Mater. Interfaces*, 2015, 5, 12058.
- 22 M. B. Qadir, K. C. Sun, I. A. Sahito, A. A. Arbab, B. J. Choi, S. C. Yi and S. H. Jeong, *Sol. Energy Mater. Sol. Cells*, 2015, 140, 141.
- 23 Y. Z. Zheng, X. Tao, L. -X. Wang, H. Xu, Q. Hou, W. -L. Zhou and J. F. Chen, *Chem. Mater.*, 2010, 22, 928.
- 24 E. Puyoo, G. Rey, E. Appert, V. Consonni and D. Bellet, *J. Phys. Chem. C*, 2012, 116, 18117.
- 25 S. Zhu, X. Tian, J. Chen, L. Shan, X. Xu and Z. Zhou, *J. Phys. Chem. C* 2014, 118, 16401.
- 26 J. Qiu, M. Guo and X. Wang, *ACS Appl. Mater. Interfaces* 2011, 3, 2358.
- 27 W. -T. Jiang, C. Te. Wu, Y. -H. Sung and J. J. Wu. *ACS Appl. Mater. Interfaces*, 2013, 5, 911.
- 28 C. -X. He, B. -X. Lei, Y. -F. Wang, C. -Y. Su, Y. -P. Fang and D. -B. Kuang, *Chem. Eur. J.* 2010, 16, 8757.
- 29 N. Memarian, I. Concina, A. Braga, S. M. Rozati, A. Vomicro and G. Sberveglieri, *Angew. Chem. Int. Ed.* 2011, 50, 12321.
- 30 C. Y. Jiang, X. W. Sun, G. O. Lo, D. L. Kwong, *Appl. Phys. Lett.*, 2007, 90, 263501.
- 31 H. -M. Cheng, W. -H. Chiu, C. -H. Lee, S. -Y. Tsai and W. -H. Hsieh, *J. Phys. Chem. C* 2008, 112, 16359.
- 32 C. Bae, H. Yoo, S. Kim, K. Lee, J. Kim, M. M. Sung and H. Shin, *Chem. Mater.*, 2008, 20, 756.
- 33 S. H. Ko, D. Lee, H. W. Kang, K. H. Nam, J. Y. Yeo and S. J. Hong, *NanoLett.* 2011, 11, 666.
- 34 M. Baghbanzadeh, L. Carbone, P. D. Cozzoli, and C. O. Kappe, *Angew. Chem. Int. Ed.*, 2011, 50, 11312.
- 35 Y. -J. Zhu and F. Chen, *Chem. Rev.*, 2014, 114, 6462.
- 36 S. Praneetha and A. VadivelMurugan, *ACS Sustainable Chem. Eng.* 2015, 3, 224.

- 37 B. Wen, Y. Huang and J. J. Boland, *J. Phys. Chem. C*, 2008, 112, 106.
- 38 Q. Zhang, S. –J. Liu and S. –H. Yu, *J. Mater. Chem.* 2009, 19, 191.
- 39 J. P. Cheng, X. B. Zhang, X. Y. Tao, H. M. Lu, Z. Q. Luo and F. Liu, *J. Phys. Chem. B*, 2006, 110, 10348.
- 40 R. Boppella, K. Anjaneyulu, P. Basak and S. V. Manorama, *J. Phys. Chem. C*, 2013, 117, 4597.
- 41 C. Pacholski, A. Kornowski and H. Weller, *Angew. Chem. Int. Ed.*, 2002, 41, 1188.
- 42 Y. Masuda and K. Kato, *Cryst. Growth Des.*, 2008, 8, 275.
- 43 J. Zhang, L. Sun, J. Yin, H. Su, C. Liao and C. Yan, *Chem. Mater.*, 2002, 14, 4172.
- 44 T. Ghoshal, S. Kar and S. Chaudhuri, *Cryst. Growth Des.*, 2007, 7, 136.
- 45 B. Li and Y. Wang, *J. Phys. Chem. C* 2010, 114, 890.
- 46 P. P. Das, S. A. Agarkar, S. Mukhopadhyay, U. Manju, S. B. Ogale and P. S. Devi, *Inorg. Chem.*, 2014, 53, 3961.
- 47 P. Rai, W-K. Kwak and Y-T. Yu, *ACS Appl. Mater. Interfaces*, 2013, 5, 3026.
- 48 W. Wang, H. Zhang, R. Wang, M. Feng and Y. Chen, *Nanoscale* 2014, 6, 2390.
- 49 Q. Wang, J. –E. Moser and M. Gratzel, *J. Phys. Chem. B*, 2005, 109, 14945.
- 50 J. Bisquert, F. Fabregat-Santiago, I. Mora-Sero, G. Garcia-Belmonte and S. Gimenez, *J. Phys. Chem. C*, 2009, 113, 17278.